

Measurement report: Radiative efficiencies of $(\text{CF}_3)_2\text{CFCN}$, $\text{CF}_3\text{OCFCF}_2$, and $\text{CF}_3\text{OCF}_2\text{CF}_3$

Beni Adi Trisna¹, Seungnam Park², Injun Park³, Jeongsoo Lee¹, Jeong Sik Lim¹

¹Greenhouse Gas Metrology team, Korea Research Institute of Standard and Science (KRISS), Science of Measurement, University of Science and Technology (UST), Daejeon 34113, Republic of Korea

²National Centre of Standard Reference Data (NCSRD), KRISS, Daejeon 34113, Republic of Korea

³Interface Materials and Chemical Engineering Research Centre, Korea Research Institute of Chemical Technology (KRICT), Daejeon 34114, Republic of Korea

Correspondence to: Jeongsoo Lee (leejs@kriss.re.kr) and Jeong Sik Lim (lim.jeongsik@kriss.re.kr)

Abstract. Absorption cross-sections of emerging greenhouse gases (GHG) were measured to estimate the radiative efficiency using high-resolution Fourier transform infrared spectroscopy (HR-FTIR). For quantitative spectroscopy, the Beer–Lambert parameters of absorber pressure, temperature, and optical path length (OPL) were accurately determined to be traceable to the primary standards. The OPL of the multipass cell mounted on the HR-FTIR spectrometer was spectroscopically calibrated. A ratio of the averaged N_2O absorptions was found to be in the range of 2217.4–2219.0 cm^{-1} , with a spectral resolution of 0.026 cm^{-1} , yielding a ratio of OPLs that falls between the multipass cell and reference cell. This cell-to-cell comparison method is free from the uncertainty in the referring line strength, which reduced the calibration uncertainty compared with the direct line-strength referring method. With the OPL-calibrated multipass cell (3.169 ± 0.079 m), the absorption cross-sections were measured at low absorber pressures with a spectral resolution of 2 cm^{-1} , integrated at 10 cm^{-1} intervals, and multiplied by the new narrow band model to yield the radiative efficiencies. The radiative efficiency values of CF_4 , SF_6 , and NF_3 were evaluated to be 0.085 ± 0.002 , 0.573 ± 0.016 , and 0.195 ± 0.008 $\text{W m}^{-2} \text{ppb}^{-1}$, respectively, which are consistent with previously reported values. For the emerging GHGs, the radiative efficiency values were determined to be 0.201 ± 0.008 $\text{W m}^{-2} \text{ppb}^{-1}$ for heptafluoroisobutyronitrile $(\text{CF}_3)_2\text{CFCN}$; commercially referred to as *Novoc-4710*), 0.328 ± 0.013 $\text{W m}^{-2} \text{ppb}^{-1}$ for perfluoro methyl vinyl ether ($\text{CF}_3\text{OCFCF}_2$; PMVE), and 0.544 ± 0.022 $\text{W m}^{-2} \text{ppb}^{-1}$ for 1,1,1,2,2-pentafluoro-2-(trifluoromethoxy)ethane ($\text{CF}_3\text{OCF}_2\text{CF}_3$; PFMEE).

1 Introduction

Radiative efficiency is a measure of the radiative forcing for a unit change in the atmospheric concentration of a single greenhouse gas (GHG). Emitted GHGs undergo degradation via a range of atmospheric reactions that define their atmospheric lifetimes. The concentration of a GHG shows a timely reduction according to its atmospheric lifetime, which also reduces the thermal energy flux. Integrating the radiative forcing over a designated time horizon yields the absolute global warming potential, which is expressed in $\text{W m}^{-2} \text{kg}^{-1} \text{yr}$. The global warming potential (GWP; unitless), defined as the ratio of the absolute GWP of a gas to the absolute GWP of CO_2 , over the same time horizon, was developed to compare the relative integrated effect of various compounds on climate. In the Nationally Determined Contribution, GHG emissions are reported in terms of the CO_2 -equivalent amount as rated by the GWP, with the value for CO_2 designated as 1 (Paris Agreement, 2015). To date,

the GWPs of major GHGs have been reported in the IPCC 6th assessment report (AR6) by combining multiple radiative forcing and atmospheric lifetime values obtained from different independent studies (IPCC, 2021). Although the GWP is the *de facto* climate metric standard for reporting the Nationally Determined Contribution, there has been a debate within the climate research community regarding the reliability of GWP values (Denison et al., 2019; Rosenzweig et al., 2018). The climate impacts of emission pathways can be misinterpreted by the simple aggregation of GWPs of different GHGs. To resolve this problem, alternative climate metrics, such as the global temperature change potential and short-lived climate pollutants adjusted GWP have been suggested to fill the error gap in the prediction of target atmospheric temperatures in the characterisation of mitigation pathways (Allen et al., 2018; Denison et al., 2019; Lynch et al., 2020). Meanwhile, the uncertainty in the measurement of GWP has gained attention as a focus area for improving the accuracy of the GWP. The IPCC AR6 includes a discussion regarding the major uncertainty sources of climate metrics that originate from the atmospheric lifetime, radiative efficiency, chemical response, and absolute GWP of CO₂ (IPCC, 2021). Sulbaek Andersen et al. (2021) determined that a standardisation of laboratory kinetics measurements is required to enhance the reliability of atmospheric lifetime measurements. Similarly, the reliability of atmospheric lifetime values can be enhanced by the accurate measurement of the absorption cross-section, which is an in-laboratory measurement parameter for radiative efficiency. According to the IPCC AR6, the uncertainties of radiative efficiency values are one of the major contributors to the total uncertainty in the GWP, with proportions of up to 22%, depending on the compound (IPCC, 2021). In this study, we propose an accurate measurement method for radiative efficiency and assess the uncertainty budget in detail.

The well-studied and emerging GHGs were comprehensively evaluated as follows: (1) The spectroscopic calibration of the optical path length (OPL) was conducted using high-resolution Fourier transform infrared spectroscopy (HR-FTIR), an essential tool for accurate absorption cross-section measurements. (2) The new narrow band model (nNBM), wherein the stratospheric-temperature adjustment has been applied to the (traditional) narrow band model (NBM), was used to evaluate the radiative efficiency. (3) An uncertainty assessment of the radiative efficiency values of the well-studied and emerging GHGs was conducted. The emerging GHGs for which the radiative efficiency values were assessed in this study were heptafluoro-isobutyronitrile (commercially known as *Novec-4710*, (CF₃)₂CFCN), 1,1,1,2,2-pentafluoro-2-(trifluoromethoxy)ethane (PFMEE, CF₃OCF₂CF₃), and perfluoro methyl vinyl ether (PMVE, CF₃OCFCF₂). *Novec-4710* is used as an alternative to SF₆ as an insulator for gas-insulated switchgear (Andersen et al., 2017; Laruelle et al., 2017; Zhao et al., 2019). PMVE and PFMEE are considered future alternatives to chlorofluorocarbons, although their RE values have rarely been reported to date (Kim et al., 2014; Li et al., 2000). The values obtained for the well-studied GHGs (NF₃, SF₆, and CF₄) were compared with those reported in previous studies to corroborate the validity of the proposed method.

2 Methods

2.1 Instrumental setup

HR-FTIR (Bruker IFS 125HR) was used throughout the measurement procedure. The spectrometer was equipped with a KBr beam splitter, which enabled measurements between 400 and 6500 cm^{-1} . The measurements were conducted by passing a collimated thermal light source through a reference gas cell or a multipass cell (the White type). A mercury cadmium telluride (MCT) detector, cooled using liquid nitrogen, was used for all the spectroscopic calibration measurements of the OPLs and absorption cross-sections of the target GHGs. For the MCT detector, a nonlinearity correction was applied to the detector response when recording the interferograms. The correction algorithm for the instrumental control and spectrum acquisition was implemented with OPUS software. For the spectroscopic calibration of the OPL, N_2O absorption spectra were obtained at a resolution of 0.026 cm^{-1} (maximum optical path difference = 36 cm) from the reference cell and multipass cell. The instrumental line shape (ILS) was retrieved from the measured N_2O spectra in the reference cell using the LINEFIT program (Fig. S1). Additionally, inverse modelling of the modulation efficiency and phase error in the domain of the optical path difference was performed (Hase et al., 1999). The pure absorption spectrum of N_2O was forward-modelled using the Voigt profile with HITRAN parameters, such as line strength and self-broadening coefficient. The residuals between the measured and modelled spectra were minimised to provide the best fits of the modulation efficiency and phase error values as a function of the optical path difference. The ILS was then reconstructed using the pre-set apodisation of the Norton–Beer strong function. Subsequently, the N_2O spectra in the multipass cell were obtained using the same instrumental parameters as those used for the reference cell measurement. The ratio of the absorption areas between the multipass cell and reference cell was obtained via deconvolution of the ILS (Fig. 1).

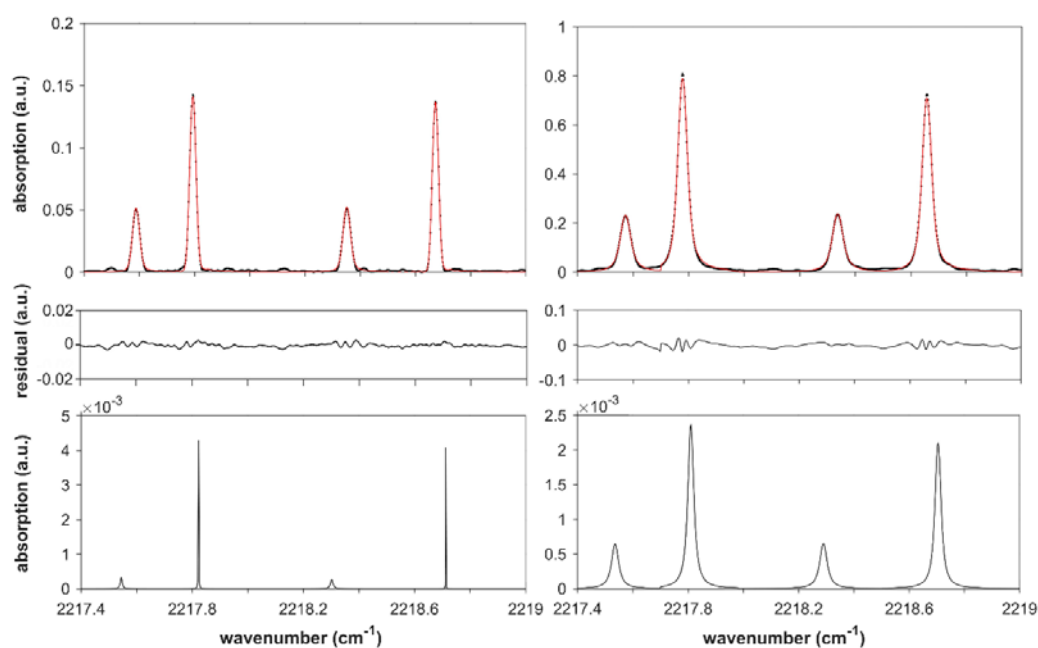
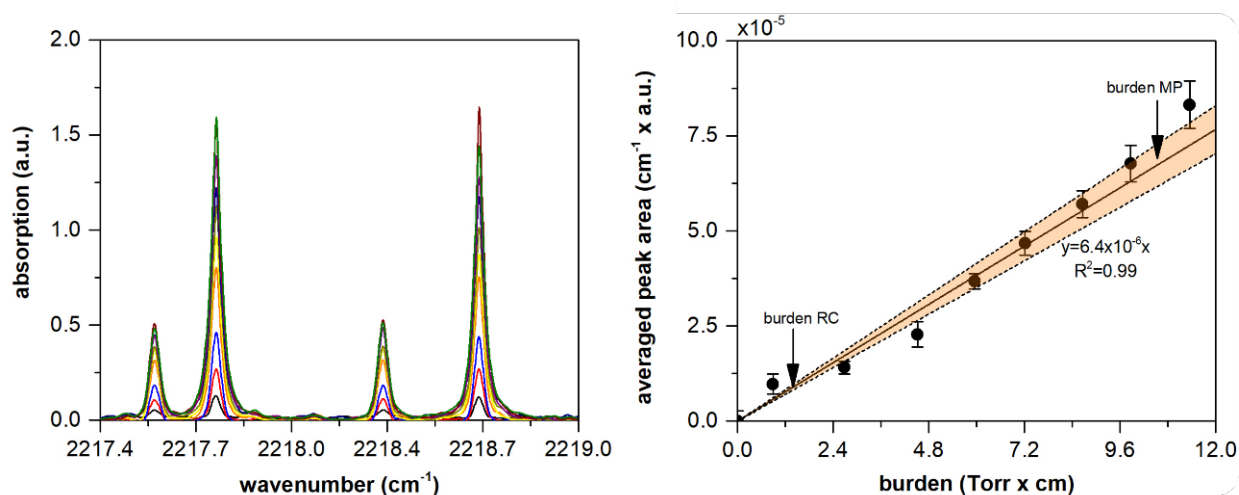


Figure 1. Instrumental line shape (ILS)-convoluted Voigt fit of the measured spectrum of the reference cell (left image in the upper row). ILS-convoluted Voigt fit of the measured spectrum of the multipass cell (right image in the upper row). The residuals of each fit are shown in the middle row of the graph. The lower row shows ILS-deconvoluted spectra of the reference and multipass cells. The areas under the ILS-deconvoluted spectra are compared, and the optical path length (OPL) of the multipass cell is determined using Eq. (4). The areas for the reference and multipass cells are 2.9×10^{-5} and 2.2×10^{-4} , respectively, resulting in an OPL of the multipass cell of 3.169 ± 0.079 m.

We found that, if the ILS was not deconvoluted, the ratio value was considerably distorted from the original value owing to the differing extents of pressure broadening. The OPL of the **multipass cell** was then determined by comparison with the peak area of the **reference cell** measurement. For this comparison, the absorption lines of N₂O were selected from 2217.4 to 2219.0

95 cm⁻¹. The theoretical details of the OPL calibration method are presented in the supplement (S1 and S2). The total pressures of the **reference** and **multipass cells** were 0.71 and 70.93 Torr, respectively. To obtain the values lying within the linear region of the curve-of-growth plot, the concentration of N₂O in the **multipass cell** was diluted to 481.943 μmol mol⁻¹ using an N₂ broadener, which corresponds to an absorption burden (OPL × partial pressure) of 10.6 cm Torr (Fig. 2). A detailed discussion of the **curve-of-growth** analysis is also provided in the supplement (S1). The length between the inner faces of the **reference**

100 **cell** (20.01 ± 0.05 mm (1σ)) is traceable to the national gauge block standards. Given that the cell temperature (297 ± 1 K) was well equilibrated to the temperature of the surroundings, it can be assumed that the temperature distribution of the gas was homogeneous throughout the beam path. The spectra were averaged 64 times.



105 **Figure 2. Absorption of N₂O with respect to cell pressure (left). The curve-of-growth plot for the corresponding peaks (right). Averaged peak areas after instrumental line shape (ILS) deconvolution are shown with respect to the absorption burden (pressure × optical path length (OPL)). Without ILS deconvolution, no linearity of fit was obtained. A weighted least squares method was employed to fit the measured dataset with a straight line crossing the origin. The orange areas represent the confidence bands (at $k = 2$) of the fitted line. The **curve-of-growth** analysis shows that the OPL calibration was valid for the cell-to-cell comparison method by occurring within the linear region of the **curve-of-growth** plot.**

110

The **absorption cross-sections** were obtained by averaging 256 spectra, measured within the wavenumber range of 500–3000 cm⁻¹, at a spectral resolution of 2 cm⁻¹. To obtain low absorption burdens at the nominal OPL of the **multipass cell**, the gases to be measured were gravimetrically diluted to a designated concentration using an N₂ broadener (the typical gravimetric uncertainty is below 1.5%). This was also required to ensure the accuracy of the pressure readings for trace levels of the

115 absorbing gas (< 0.1 Torr) using pressure gauges, the full scales of which are over 100 Torr (accuracy of 0.05 Torr) with a valid dynamic range of 5% to 95% (Johnson et al., 2021). The overall signal-to-noise ratios (S/N) of the absorption spectra were higher than 2000. NF₃ at a pressure of 0.035 Torr was mixed with N₂ to yield a total pressure of 354.97 Torr in the

120 [multipass cell](#). In brief, the partial pressures for SF₆, CF₄, PMVE, and PFMEE were 0.0057, 0.021, 0.047, and 0.039 Torr, respectively, using N₂ as the broadening agent. For *Novec*-4710, the partial pressure was set at 0.11 Torr and broadened using CO₂. The pressure gauges (INFICON, CDG025D, and MKS, 626A13TBE) were calibrated against the standards set by the Korea Research Institute of Standard and Science (KRISS). The temperature sensors (Testek, 303A and SK Sato, PC-5000TRH-II) were calibrated against a platinum resistance thermometer (Fluke-Hart Scientific, 5628) that was traceable to the NIST temperature fixed-point standards. The other instrumental parameters for the OPL calibration and [absorption cross-section](#) measurements are listed in Table 1.

125 **Table 1. Instrumental setup and experimental conditions**

Parameter	OPL calibration		Absorption cross-section measurement
	Reference cell (N ₂ O)	Multipass cell (N ₂ O)	
Spectral range measured	6500–500 cm ⁻¹	6500–500 cm ⁻¹	6500–500 cm ⁻¹
Spectral resolution	0.025 cm ⁻¹	0.025 cm ⁻¹	2 cm ⁻¹
Light source	SiC Globar	SiC Globar	SiC Globar
Collimator focal length	418 mm	418 mm	418 mm
Optical speed	<i>f</i> /6.5	<i>f</i> /6.5	<i>f</i> /6.5
Beam splitter	KBr	KBr	KBr
Detector	LN ₂ -cooled MCT	LN ₂ -cooled MCT	LN ₂ -cooled MCT
Gas cell	Glass single-pass cell 20.01 mm	Glass multipass cell 3100 mm (max. 28,000 mm)	Glass multipass cell 3100 mm (max. 28,000 mm)
Optical path length	20.01 mm	3100 mm	3100 mm
Mirror velocity	60 kHz	60 kHz	60 kHz
Acquisition mode	Single-sided, Forward-Backward	Single-sided, Forward-Backward	Single-sided, Forward-Backward
Jacquinot aperture	2 mm	2 mm	4 mm
Laser wavenumber	15,798.015 cm ⁻¹	15,798.015 cm ⁻¹	15,798.015 cm ⁻¹
Number scan sample	64	64	256
High-pass filter	Open	Open	Open
Low-pass filter	20 kHz	20 kHz	20 kHz
Preamplifier gain	2 kHz	2 kHz	2 kHz
Switch gain	n/a	n/a	n/a
High freq. limit	15,798	15,798	15,798
Low freq. limit	0	0	0
Phase resolution	2 cm ⁻¹	2 cm ⁻¹	2 cm ⁻¹
Phase correction	Mertz	Mertz	Mertz

Apodisation mode	Norton–Beer, Strong	Norton–Beer, Strong	Boxcar
Zero filling factor	8	8	32
Pressure gauge	n/a	MKS 626A	INFICON CDG025D and MKS 626A
Partial (total) pressures	0.7 Torr (0.7 Torr)	0.034 Torr (70.93 Torr)	See main text
Burdens (pressure × OPL)	1.4 cm·Torr	10.6 cm·Torr	See main text

2.2 Spectroscopic calibration method for the optical path length

Quantification of gas absorption requires Beer–Lambert parameters, such as pressure, temperature, and OPL. In this study, the pressures and temperatures were measured directly. The OPL of the [multipass cell](#) was calibrated based on FTIR spectroscopy, and its uncertainty was assessed by applying the linear law of propagation of uncertainty (JCGM, 2008). The absorbance measured at high pressures exhibited a different extent of saturation according to the respective bands, disobeying the linear property of the Beer–Lambert law (Johnson et al., 2021). Therefore, it was critical to use the [multipass cell](#) at low partial pressures. However, a single pass cell is frequently used with a (sometimes mechanically determined) preassigned OPL uncertainty or only the nominal OPL value (Harrison et al., 2010; Harrison, 2015; Harrison, 2020; Robson et al., 2006). However, measuring the OPL of a [multipass cell](#) requires an alternative approach rather than the mechanical method used for measuring the OPL of a single-pass cell. In this regard, Nwaboh et al. (2014) demonstrated a calibration method for the OPL of a [multipass cell](#) using tunable diode laser absorption spectroscopy (TDLAS), in which the OPL and absorption are related as follows:

$$x_{abs} = \frac{k_B \cdot T}{S_T \cdot L \cdot P_{abs}} \cdot A_{abs}, \quad (1)$$

where x_{abs} is amount fraction of absorber, k_B is the Boltzmann constant, T is the temperature, S_T is the line strength of the probed absorption line, r_{iso} is the isotope abundance of absorbing N_2O , L is OPL, P_{abs} is the partial pressure of the absorber, and A_{abs} is the integrated peak area under the absorption line of the absorbing gas ($\int_{-\infty}^{\infty} A_{meas}(\tilde{\nu} - \tilde{\nu}_0) d\tilde{\nu}$), where $\tilde{\nu}_0$ is the center transition wavenumber. Using Eq. (1), L_{MP} can be obtained directly by comparing the referred line strength, hereafter referred to as the direct line-strength referring method. Nwaboh et al. (2014) reported the OPL calibration result of the gas cell against a line strength of CH_4 as 4987.3 cm^{-1} ($(8.289 \pm 0.414) \times 10^{-22} \text{ cm}^{-1} / (\text{cm}^{-2} \cdot \text{molecule})$), and contribution of 95.4% to the standard uncertainty of OPL, which led to a relative standard uncertainty of 5%. A similar phenomenon has been reported in the calibration of gas concentrations (x_{abs}) using cavity ringdown spectroscopy (CRDS), wherein the expected value of the OPL was substituted by the direct measurement of the ringdown time. Consequently, the calibration of x_{abs} against S_T in the CRDS measurements is analogous to the OPL calibration in the TDLAS measurement. The uncertainty in S_T contributed to over 80% of the standard uncertainty in x_{abs} , which was 1.2% of the calibrated value (Kim et al., 2021). The findings of these

studies implied that the direct line-strength referring method needs to be bypassed to avoid direct use of the line strength, which in classic line databases, such as HITRAN and GEISA, exhibits a non-negligible or considerably high uncertainty.

155 Instead, we attempted to construct a measurement traceability chain of the OPL of the **multipass cell** L_{MP} to the national gauge block using the cell-to-cell comparison method. In this method, line strength acts as a mediator between the measurements of the **reference and multipass cells** (Nwaboh et al., 2014). The uncertainty of OPL of the **reference cell** L_{RC} (0.12%, including the measurement uncertainty using callipers) was better than that of the referred line strengths. Although experimentally determined uncertainties of the referred N_2O lines in this study, (0111) ← (0110) R9e (first peak), (0001) ← (0000) P7e

160 (second peak), (0111) ← (0110) R10e (third peak), and (0001) ← (0000) P6e (fourth peak), have not been reported (Table S3), those of N_2O have typically been reported to be between 2% and 5% within the measurement range of 0–3000 cm^{-1} (Gordon et al., 2017; Pinnock and Shine, 1998). Notably, other GHGs, such as CO_2 and CH_4 , have exhibited similar levels of uncertainty. As discussed in Section 3.1, the uncertainties of the referred line strengths were not required in the uncertainty evaluation process.

165 An optical bandpass filter at a central wavelength of 4.5 μm was used to measure the spectra obtained from the **reference cell**. The optical bandpass filter in front of the **reference cell** enabled the setting of similar radiant powers transmitted through both the **multipass** and **reference cells** because the throughput of the **multipass cell** was reduced to 80% owing to the surface aging of the gold reflection mirrors. This ensured that the interferograms of the **reference** and **multipass cells** were obtained at the same aperture size of 2 mm and at similar S/N levels. The identical field-of-view function (same aperture size) between

170 multiple measurements was required to ensure identical ILSs for the comparison of the **multipass** and **reference cell** measurements (Smith et al., 2011). We assumed that no significant drift in the ILS occurred during the entire measurement process. The boxcar apodisation function should yield a sharper ILS that resembles the sinc function at the set maximum optical path difference. However, the Norton–Beer strong function provides a reasonable symmetric line shape by effectively suppressing the sideband even at a less ideal alignment status of the interferometer.

175 The spectral absorption $A(\tilde{\nu})$ was calculated as $-\ln(\Phi(\tilde{\nu})/\Phi_0(\tilde{\nu}))$, where $\Phi(\tilde{\nu})$ and $\Phi_0(\tilde{\nu})$ are the transmitted and incident radiant powers, respectively. The measured spectral absorbance at the transition wavenumber $\tilde{\nu}_0$, $A_{meas}(\tilde{\nu})$, can be expressed by the convolution of the pure gas absorption line $A_{pgs}(\tilde{\nu})$ and the ILS as follows:

$$A_{meas}(\tilde{\nu}) = A_{pgs}(\tilde{\nu}) \otimes ILS(\tilde{\nu}) \quad (2)$$

180

Therefore, in FTIR spectroscopy, A_{abs} is the integrated area under the ILS-deconvoluted absorption line of the absorbing gas, namely, $\int_{-\infty}^{\infty} A_{pgs}(\tilde{\nu} - \tilde{\nu}_0) d\tilde{\nu}$. In contrast, using TDLAS, an ILS of less than a few megahertz could be treated as a delta function because the linewidths of the well-separated absorption lines of a small molecule are typically over a few gigahertz. This aspect of laser-based measurements simplifies the procedure of OPL calibration, which is facilitated by the direct

185 measurements of the [reference](#) and [multipass cells](#) without the retrieval of the pure gas spectra. Because the linewidth of the FTIR ILS obtained in the present study was comparable to that of the pure gas absorption line, the peak area measured using FTIR spectroscopy was substantially distorted from that of the pure gas absorption line. Mathematically, for a comparison of the integrated area, the convoluted functions of the numerator and denominator cannot be cancelled ($\frac{\int a(x)}{\int b(x)} \neq \frac{\int a(x) \otimes c(x)}{\int b(x) \otimes c(x)}$). Based on Eq. (1), L_{MP} was obtained by comparing the spectral absorptions of the [reference](#) and [multipass cells](#), and is expressed as
 190 follows:

$$L_{MP} = \frac{T_{MP} \cdot P_{RC} \cdot L_{RC} \cdot A_{MP} \cdot S_{T,RC}}{T_{RC} \cdot P_{MP} \cdot A_{RC} \cdot S_{T,MP}} \quad (3)$$

where S_T comprises the temperature-dependent prefactor (P_T) and reference line strength (S_0), as described in the supplement
 195 (S3). The peak areas of the pure gas spectra of the [multipass](#) and [reference cells](#) (A_{MP} and A_{RC} , respectively) were estimated using the trapezoidal method. The peak areas fell within the linear region of the [curve-of-growth](#) plot, ensuring the accuracy of this calibration method by securing linearity (Fig 2). However, the uncertainty of the slope of the [curve-of-growth](#) plot must also be included in the uncertainty of A_{MP} (S2). The partial pressure of the broadener was not a factor in determining the values of A_{MP} and A_{RC} .

200 2.3 Estimation of radiative efficiency

[Radiative efficiency](#) is a measure of the radiative forcing for a unit change in the atmospheric concentration of a gas, and is generally reported in $\text{W m}^{-2} \text{ppb}^{-1}$. To obtain the [radiative efficiency value](#), the [absorption cross-section](#) of a GHG is multiplied by the [radiative forcing](#) as follows:

$$205 \quad RE = \sum_{i=1}^{250} RF_i \cdot \sigma_i(\tilde{\nu}, P_{abs}, T), \quad (4)$$

where RF_i is the applied [radiative forcing](#) model and $\sigma_i(\tilde{\nu}, P_{abs}, T)$ is the integrated [absorption cross-sections](#) at the i -th wavenumber block. The instantaneous radiative forcing model, which accounts for the global and annual means of the Earth's atmosphere, was proposed by Pinnock et al. (1995). The Pinnock curve is based on a 10 cm^{-1} narrow-band model. Hodnebrog
 210 et al. (2013) subsequently updated the Pinnock curve by increasing the spectral resolution from 10 to 1 cm^{-1} using the Oslo line-by-line radiative transfer code at a spectral resolution of 0.02 cm^{-1} , hereafter referred to as the high-resolution narrow band model (hNBM). Although the Oslo line-by-line model includes an improved representation of the water vapor continuum and some changes to the representation of clouds, it is computationally expensive to introduce the necessity of a parameterised radiative forcing model such as a narrow band model (NBM, Hodnebrog et al., 2020; Shine and Myhre, 2020). In the new
 215 NBM (nNBM) proposed by Hodnebrog et al. (2020), the effect of the stratospheric temperature adjustment was added to the

NBM. Notably, in the studies conducted by Hodnebrog et al., a lifetime correction for short-lived species was applied to improve the breakdown of the baseline assumption, which accounts for the well-mixed condition of a stable GHG within the atmosphere. In the present study, we applied the nNBM without lifetime correction. σ_i is the integrated **absorption cross-section** obtained at a spectral resolution of 2 cm^{-1} and integrated at a 10 cm^{-1} block interval. We did not observe any dependence
 220 of the **radiative efficiency** values on the spectral resolution of the **absorption cross-section**, which tends to imply a negligible effect of the variation in the linewidth of the ILS on the value of the **integrated absorption cross-section**. Johnson et al. (2021) demonstrated that **the integrated absorption cross-sections** of isobutane measured at multiple resolutions between 0.01 and 4.0 cm^{-1} were in good agreement, thereby implying that resolution dependence did not need to be considered. This confirms that the **radiative efficiency** is an **integrated absorption cross-section** that is weighted by a radiative forcing model from 0 to 3000 cm^{-1} . Above 3000 cm^{-1} , solar radiation is strongly reduced in the atmosphere, thus indicating that laboratory-measured **absorption cross-section** values exceeding 3000 cm^{-1} do not influence **radiative efficiency** value (Pinnock et al., 1995); $\sigma_i(\tilde{\nu}, P_{abs}, T)$ is expressed as follows (Harrison et al., 2010; Harrison, 2015; Harrison, 2020):

$$\sigma_i(\tilde{\nu}, P_{abs}, T) = \frac{10^4 \cdot k_B \cdot T}{L_{MP} \cdot P_{abs}} \ln \left(\frac{\Phi_{0,i}(\tilde{\nu})}{\Phi_i(\tilde{\nu}, P_{abs}, T)} \right) \quad (5)$$

230

The absorption cross-section is expressed in terms of $\text{cm}^2 \text{ molecule}^{-1}$. Owing to instrumental limitations, we did not measure **absorption cross-sections** below 500 cm^{-1} in the present study, which may have introduced additional uncertainty in the **radiative efficiency** value for cases in which these absorption bands occur (Hodnebrog et al., 2013).

3 Results and Discussion

235 3.1 Calibration of optical path length

Figure 2 shows the measurement results of the spectroscopic calibration of L_{MP} . According to Eq. (3), the ratio of A_{MP} to A_{RC} results in L_{MP} at a given pressure and temperature. In our study, four absorption lines from 2217.4 to 2219.0 cm^{-1} were simultaneously fitted to minimise the fit residuals. In this 'multispectra fitting' method, each peak was modelled using the **Voigt** profiles with a fixed Doppler width (g_D), independent Lorentzian widths (g_L), and peak areas (A_{abs}). This is because the
 240 Doppler width depends only on the temperature and molecular weight, which are universal for every absorption line. In contrast, g_L and A_{abs} are inherent parameters of each absorption line. In every optimisation step, the retrieved ILS $ILS(\tilde{\nu})$ was convoluted to the modelled pure gas spectrum $A_{pgs}(\tilde{\nu})$, and the residuals between the measured and modelled spectra were minimised to obtain the best fit for the spectral parameters (A_{abs}, g_L, g_D). The measurement of the pressure broadening coefficient was beyond the scope of this study because the peak area was not affected by pressure broadening. Because the
 245 temperature variations in the **multipass** and **reference cells** during the experiments are independent of each other, the

uncertainties in $S_{T,RC}$ and $S_{T,MP}$ should be independently determined (S3). The combined standard uncertainty in L_{MP} was estimated based on the general law of uncertainty propagation and the derivation of Eq. (3) as follows (JCGM, 2008):

$$ru^2(L_{MP}) = ru^2(A_{MP}) + ru^2(A_{RC}) + ru^2(P_{T,MP}) + ru^2(P_{T,RC}) + ru^2(L_{RC}) + ru^2(T_{MP}) + ru^2(T_{RC}) + ru^2(P_{MP}) + ru^2(P_{RC}), \quad (6)$$

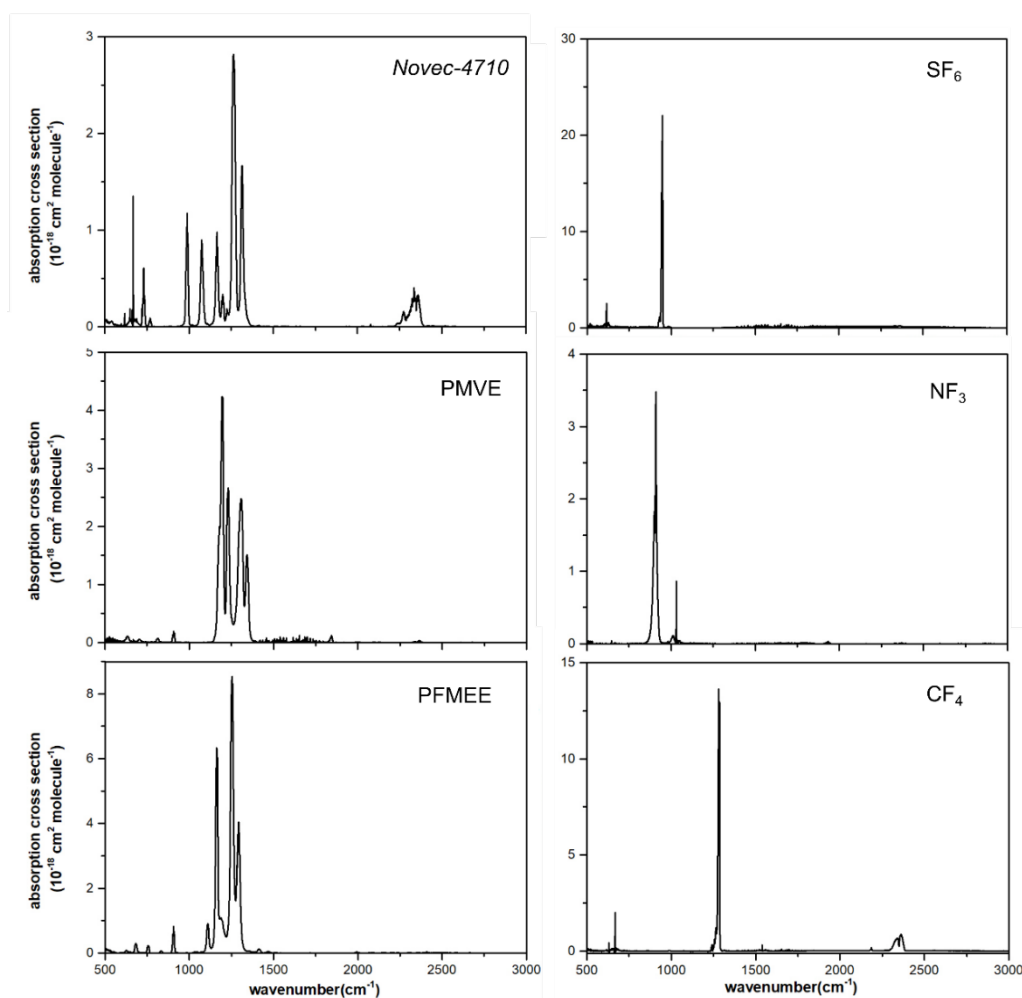
where ru is the relative uncertainty. An advantage of the [cell-to-cell comparison](#) method is indicated in Eq. (6). Because the S_0 values of $S_{T,RC}$ and $S_{T,MP}$ are fully correlated ($\rho = 1$), $u(S_0)$ is cancelled by the negative definite covariance, namely $u^2(S_0) + u^2(S_0) - 2 \cdot cov(S_0, S_0) = 0$ (details are provided in S2) (Nwaboh et al., 2014). This approach is identical to the uncertainty assessment method applied in isotope dilution mass spectrometry (Pagliano and Meija, 2016). To determine the uncertainty in the P_T and $u(P_T)$, the thermodynamic (partition function and Boltzmann population) and quantum chemical (energy level) properties were weighted by the temperature. Details regarding the uncertainty evaluation method used for each term are described in the supplement (S2). In brief, the most sensitive sources of the OPL uncertainty were the absorption peak areas and L_{RC} , whereas the contributions by L_{MP} were similar to those of the other uncertainty sources, such as temperature and pressure variations. The uncertainties of the absorption peak areas could be assigned to the instrumental origin. As shown in Fig. 1, clear undulating patterns in the fit residuals imply that the S/N ratio was sufficiently high to eliminate the white noise generated by the MCT detector. However, the undulations in the fit residuals (0.10% for [multipass cell](#) and 0.13% for [reference cell](#)) were caused by the non-ideal ILS. An uneven sampling period, i.e. [phase error](#), and transversal displacement of the retroreflector, i.e. [modulation efficiency](#), during interferogram acquisition, both leading to a non-ideal ILS, are deemed to be critical factors affecting the fit residuals, considering that the [Voigt](#) profile fits the absorption line shape of N_2O especially well in the measured wavenumber range (Loos et al., 2015). It was also noted that the uncertainty of the slope of the [curve-of-growth](#) plot, $u(COG_{slope})$, was added to the uncertainty of A_{MP} to account for the comparability between the distinct values of L_{MP} and L_{RC} . The $u(COG_{slope})$ was found to contribute to up to 80% of $u(L_{MP})$. The slope of the [curve-of-growth](#) plot was determined using the weighted least squares method with a straight line that crosses the origin. Consequently, we obtained values of 3.169 ± 0.079 m for L_{MP} . The associated uncertainty budget is presented in Table S1.

3.2 Radiative efficiencies and associated uncertainties of emerging greenhouse gases

Figure 3 shows the [absorption cross-sections](#) of the emitted GHGs. The uncertainty in the [radiative efficiency](#) could be evaluated based on the law of uncertainty propagation from the derivation of Eq. (5) (JCGM, 2008). Assuming that all the uncertainty components are independent, the relative uncertainty in the [radiative efficiency value](#), $ru(RE)$, can be estimated as follows:

$$ru^2(RE) = ru^2(L_{MP}) + ru^2(P) + ru^2(x) + ru^2(T) + 2 \cdot ru^2(rd) \quad (7)$$

where $ru(L_{MP})$, $ru(rd)$, $ru(P)$, and $ru(T)$ are the relative uncertainties of the L_{MP} , responsivity drift, total pressure measurement, and temperature variability, respectively. The responsivity drift of the FTIR spectrometer occurred as a variation of the measured radiance of the light source. This drift can occur owing to various causes, such as the temporal variation in the radiant intensity of the light source, and the detection sensitivity. These uncertainty components were evaluated as described in Section 3.1. Finally, $ru(x)$ is the uncertainty of the amount fraction of the absorbing gas. The partial pressure of the absorber is $P \times x$. Although the band shape generally varies depending on the temperature, the integrated absorption cross-sections may remain constant within the measured temperature range, leading $\Phi_i(\tilde{\nu}, P_{abs})$ (Harrison et al., 2020; Nelson et al., 2012). Therefore, the temperature terms in Eq. (5) were only dependent on the prefactor. We did not consider the uncertainty of nNBM because the values were not reported in the previous study. A hidden uncertainty source may be the lack of data for bands below 500 cm^{-1} in the present study. For example, the missing bands in the far infrared region may cause a systematic bias in the radiative efficiency value, as larger compounds exhibit low-frequency bending vibrations (Bravo et al., 2010).



290

Figure 3. Absorption cross-section measurements for estimating the radiative efficiencies of heptafluoroisobutyronitrile (*Novec-4710*) at $297.15 \pm 1 \text{ K}$, perfluoro methyl vinyl ether (PMVE) at $297.15 \pm 1 \text{ K}$, 1,1,1,2,2-pentafluoro-2-(trifluoromethoxy)ethane (PFMEE) at $295.15 \pm 1 \text{ K}$, SF_6 at $297.15 \pm 1 \text{ K}$, NF_3 at $296.15 \pm 1 \text{ K}$, and CF_4 at $296.15 \pm 1 \text{ K}$.

3.2.1 Well-studied greenhouse gases

295 To validate the proposed methods in the present study, the radiative efficiencies of SF₆, CF₄, and NF₃ were estimated and compared with those reported in the literature, with absorption burdens of 1.8, 6.6, and 11.2 cm Torr, respectively. Numerous studies have reported the radiative efficiency values of GHGs obtained using different radiative forcing models. In Hodnebrog et al. (2013), the radiative efficiency values of SF₆ were found to be within the range of 0.49–0.68 W m⁻² ppb⁻¹, depending on the radiative forcing model used (with a mean value of 0.56 W m⁻² ppb⁻¹). In the same study, the authors used hNBM with the lifetime correction to obtain a radiative efficiency estimate of 0.57 W m⁻² ppb⁻¹, which is consistent with the value obtained in the present study (0.573 ± 0.02 W m⁻² ppb⁻¹) using the nNBM. In another study by Hodnebrog et al. (2020), the radiative efficiency value with the nNBM and lifetime correction was also 0.57 W m⁻² ppb⁻¹, which is consistent with that obtained in the current study. Although the value obtained in the present study was not lifetime-corrected, this consistency between studies validates our proposed method, considering that lifetime correction for long-lived GHGs is generally considered ineffective, owing to their long atmospheric lifetime (e.g. 3,200 years for SF₆), which facilitates a well-mixed atmospheric condition. The IPCC AR6 adopted a radiative efficiency value of 0.567 W m⁻² for SF₆, which is also in good agreement with the present study (IPCC, 2021). Similar relationships were identified for NF₃ and CF₄, which have long lifetimes of 740 and 50,000 years, respectively. (Table 2) However, the radiative efficiency value of SF₆ reported by Jain et al. (2000), who used the NBM, showed a considerable decrease compared with the values of SF₆, NF₃, and CF₄ obtained in other studies. In practice, the radiative forcing intensity in the 700–1000 cm⁻¹ range of the NBM is decreased in comparison with that of the nNBM (Shine et al., 2020). In the same region, a strong band of SF₆ spikes, which might contribute to the considerable decrease in the NBM-based radiative efficiency value of SF₆. Detailed uncertainty budgets for SF₆, NF₃, and CF₄ are presented in Tables S3, S4, and S5, respectively.

315 **Table 2. Summary of the radiative efficiency values obtained in this study and previous studies. The confidence level of uncertainty of the radiative efficiency value in this study is 95%.**

	Radiative efficiency (Wm ⁻² ppb ⁻¹)							
	This work (<i>k</i> = 2)	Hodnebrog <i>et al.</i> (2013)	Hodnebrog <i>et al.</i> (2020)	IPCC AR6	Jain <i>et al.</i>	Kovac <i>et al.</i>	Andersen <i>et al.</i>	Li <i>et al.</i>
SF ₆	0.573 ± 0.016	0.57	0.57	0.567	0.49	0.59		
CF ₄	0.085 ± 0.002	0.09	0.10	0.099	0.088			
NF ₃	0.195 ± 0.008	0.21	0.20	0.204				
<i>Novec-4710</i>	0.201 ± 0.008						0.223 ¹⁾	
PMVE	0.328 ± 0.013							0.0463
PFMEE	0.544 ± 0.022				No data available			
RF Model	nNBM	hNBM (w/ τ correction) ²⁾	nNBM (w/ τ correction)	compiled	NBM	RFM	nNBM	2D-CTM
Range (cm ⁻¹)	500–3,000	500–2,500	500–3,000	compiled	500–2,500	500–2,000	500–2,500	500–2,500

- 1) The final value was cited as $0.217 \text{ W m}^{-1} \text{ ppb}^{-1}$, which was lifetime corrected.
- 2) τ correction denotes lifetime correction

3.2.2 *Novec-4710*

Among the range of emerging GHGs, *Novec-4710* is considered to be a sustainable replacement for strong gas insulators such as SF_6 . Its superior dielectric properties but low GWP make it desirable as an insulating material for eco-friendly gas-insulated switchgear (Pan et al., 2020). *Novec-4710* was gravimetrically diluted with a CO_2 broadener to a concentration of $39,967 \mu\text{mol mol}^{-1}$. In contrast to the other gases measured, CO_2 was used as the broadener for *Novec-4710* for practical reasons, because a *Novec-4710*/ CO_2 mixture has been used in the dielectric medium used in eco-friendly gas-insulated switchgear. Nevertheless, we assumed that the **integrated absorption cross-section** of *Novec-4710* does not **differ** from that obtained when using an N_2 broadener. In general, the extent of alien gas broadening is considerably smaller than that of self-broadening (Johnson et al., 2021). The **absorption cross-section** of *Novec-4710* is shown in Fig. 3. The absorption burden for the **absorption cross-section** measurement of *Novec-4710* was found to be 35.6 cm Torr. Our results revealed that bands in the range of $865\text{--}1355 \text{ cm}^{-1}$ contributed to almost 90.8% of the **radiative efficiency** value, whereas minor bands in the range of $600\text{--}785 \text{ cm}^{-1}$ contributed an additional 5.1%. Compared with the estimated **radiative efficiency** value of $0.217 \text{ W m}^{-2} \text{ ppb}^{-1}$ obtained previously by **Sulbaek** Andersen et al. (2017) using an nNBM model, we obtained a value of $0.201 \pm 0.008 \text{ W m}^{-2} \text{ ppb}^{-1}$, which accordingly implies unresolved uncertainty sources. A detailed uncertainty budget for *Novec-4710* is presented in Table 3.

3.2.3 Perfluoro methyl vinyl ether and 1,1,1,2,2-pentafluoro-2-(trifluoromethoxy)ethane

PMVE is used to develop novel fluoroplastics and fluorine rubber, although its climatic impacts have yet to be sufficiently assessed. PMVE was synthesised in our laboratory and broadened using N_2 as a broadener. Owing to its high flammability, handling with N_2 dilution was essential. The absorption burden during the **absorption cross-section** measurement of PMVE was estimated to be 14.8 cm Torr. Li et al. (2000) reported that the **radiative efficiency** value of PMVE was $0.0499 \text{ W m}^{-2} \text{ ppb}^{-1}$ using a two-dimensional chemical transport model (2D-CTM) that evaluated a change in the radiative forcing due to a change in the concentration derived by a modelled vertical decaying profile. The **radiative efficiency** value of PMVE estimated with **chemical transport models** showed a noticeable underestimation, compared with the present study. The **absorption cross-section** of PMVE obtained in the present study was found to be 1.5 times greater at the strongest band compared with that reported by Li et al., whereas our estimated **radiative efficiency** value of $0.328 \text{ W m}^{-2} \text{ ppb}^{-1}$ is 6.8-fold larger than that estimated by Li et al. (2000), confirming the underestimation tendency of the 2D-CTM. The significant contribution of **radiative forcing** to PMVE is from the bands within $1135\text{--}1365 \text{ cm}^{-1}$ (93.1%). An uncertainty budget for PMVE is presented in Table S6.

PFMEE is a prospective substitute for chlorofluorocarbons, the absorption burden during the **absorption cross-section** measurement of which was estimated to be 12.4 cm Torr. PFMEE was synthesised in our laboratory and broadened using N_2 as a broadener. Our findings reveal that bands in the range of $1035\text{--}1325 \text{ cm}^{-1}$ contributed almost 91.8% to the **radiative efficiency** value, and the minor bands at $615\text{--}925 \text{ cm}^{-1}$ contributed 7.1% to the **radiative efficiency** value. To the best of our

knowledge, the **radiative efficiency** value of PFMEE, which we estimated to be $0.544 \pm 0.022 \text{ W m}^{-2} \text{ ppb}^{-1}$, is reported for the first time. Although the overall band shapes of PMVE and PFMEE do not appear to be similarly weighted by the **radiative forcing** model, the **absorption cross-section** intensities of PFMEE at $1000\text{--}1500 \text{ cm}^{-1}$ were found to be 2-fold higher than those of PMVE, accordingly yielding 2-fold higher **radiative efficiency** values. This difference can be attributed to the C=C bonds of PFMEE, which strengthen the structural rigidity and enhance the Franck–Condon overlap integral. The uncertainty budget for PFMEE is presented in Table S7.

Table 3. Uncertainty budget for radiative efficiency of *Novec-4710* (representative example, others are presented in the supplement)

Sources	Symbol	Relative uncertainty (%), $k = 1$	Sensitivity coefficient	DOF	Distribution	Type	Contribution (%)
OPL of MP ¹⁾	$ru(L_{MP})$	1.3	-6.3×10^{-4}	∞	Normal	B	38.33
Pressure	$ru(P)$	0.047	-0.071	4	Student's t	A	0.05
Temperature	$ru(T)$	0.194	6.8×10^{-4}	∞	Uniform	A	0.93
Amount fraction	$ru(x)$	1.5	-5.0	∞	Normal	B	55.19
Responsivity drift	$ru(rd)$	0.474	5.2	∞	Normal	B	5.51
Combined uncertainty	$ru(RE)$	2.02		∞	Normal	-	100

1) A detailed budget is provided in the supporting information

4 Conclusion

In this study, a **radiative efficiency** value for PFMEE, an emerging GHG, is reported for the first time. Additionally, we re-evaluated the RE values of NF_3 , SF_6 , *Novec-4710*, CF_4 , and PMVE. Moreover, the utility of a metrology-level measurement of **absorption cross-section**, performed in conjunction with a direct calibration of L_{MP} mounted in the HR-FTIR spectrometer, is demonstrated for the first time. The **radiative efficiency** values of the well-studied GHGs obtained in this study are consistent with those reported in previous studies, thereby demonstrating the validity of the proposed method. Although the use of different **radiative forcing** models can introduce subtle deviations in the **radiative efficiency** values, the proposed method contributes to reducing the uncertainty of **radiative efficiency** value. The present study establishes measurement traceability to the primary standards for the Beer–Lambert parameters of temperature, pressure, and OPL, which ensure the reliability of the reported **radiative efficiency** values. The **cell-to-cell comparison** method exhibited a 2.5% uncertainty (at 95% confidence level) for the spectroscopic calibration of the OPL, which contributes approximately 35% to the standard uncertainty of **radiative efficiency** value. Notably, the dead length within a **multipass cell** is often missed in the product specification, thereby resulting in a systematic error in the evaluation of the OPL (Nwaboh et al., 2014). The **cell-to-cell comparison** was unaffected by the S_T of the referred lines but was sensitive to L_{RC} . Meanwhile, a highly accurate S_T enables the reduction in the $u(L_{MP})$ with a combination of the direct line-strength referring method, which does not require a **curve-of-growth** analysis. Metrological spectroscopic measurements, such as frequency-stabilised cavity ring-down spectroscopy, are a potent tool for establishing line strength with high accuracy (Fleisher et al., 2019).

Another consideration is the significance of the partial pressure of the absorbing gas. As shown in Table 3, the uncertainty in the amount fraction (partial pressure \times concentration) contributes approximately 50% to the standard uncertainty of the radiative efficiency value. Because low-pressure measurements of the absorption cross-section are required to ensure that no systematic errors arise from the saturation effect, using a multipass cell and a pressure broadener is essential. As typical pressure sensors are valid within a dynamic range of 5% to 95%, the pressure added by a broadening agent enhances the accuracy of the pressure reading. However, further improvements in the dilution uncertainty can be achieved by using metrology-level gravimetry (Rhoderick et al., 2014).

One of the uncertainty sources that we were able to control is the responsivity drift of the FTIR spectrometer, which corresponded to a 5% contribution to the standard uncertainty of the radiative efficiency value. In the quality assurance/quality control process, a high sensitivity coefficient implies that the corresponding measurement parameter should be carefully controlled to improve the measurement quality. Although the sensitivity coefficients of the responsivity drift were 10^4 -fold higher than those of OPL calibration, our measurements restricted the corresponding uncertainty well. However, the responsivity drift can be improved by bracketing the Φ_0 and Φ measurements.

New GHG substituents and their relevant applications are expected to be actively developed in the coming years, reflecting the continuing drive to replace potent GHGs (e.g., NF_3 , SF_6 , and CF_4). However, these may have short atmospheric lifetimes, and thus high chemical activity. Such compounds should therefore be handled with care by diluting them using inert gases. Therefore, we believe that the method proposed herein will be beneficial for improving the laboratory measurement procedures for determining radiative efficiency. In future studies, we intend to extend the measuring window into the far infrared range, in which absorption bands contribute approximately 3% to the total radiative forcing uncertainty (Hodnebrog et al., 2020).

Data Availability

Data are available at <https://doi.org/10.5281/zenodo.7132870> (Beni, 2022).

Supplement

S1. Curve-of-growth measurement for optical pass length calibration of multipass cell.

S2. Uncertainties in fitted peak area and curve-of-growth slope.

S3. Parametric evaluation of uncertainty in radiative efficiency value.

Fig. S1. Instrumental line shape reconstruction results from the N_2O spectrum measurement.

Fig. S2. Responsivity drift measurement.

Table S1. Uncertainty budget of optical pass length calibration of multipass cell.

Table S2. Referred line data for optical pass length calibration of multipass cell.

Table S3. Uncertainty budget of the radiative efficiency value of NF_3 .

Table S4. Uncertainty budget of the radiative efficiency value of SF_6 .

Table S5. Uncertainty budget of the radiative efficiency value of CF₄.

405 Table S6. Uncertainty budget of the radiative efficiency value of perfluoro methyl vinyl ether (PMVE).

Table S7. Uncertainty budget of the radiative efficiency value of 1,1,1,2,2-pentafluoro-2-(trifluoromethoxy)ethane (PFMEE).

Author Contributions

Study design: Jeong Sik Lim, Jeongsoon Lee

Methodology establishment: Jeong Sik Lim, Beni Adi Trisna

410 Measurement: Beni Adi Trisna

Gas synthesis and preparation: Injun Park

Data analysis and uncertainty evaluation: Beni Adi Trisna

Supervision: Jeong Sik Lim, Jeongsoon Lee

Validation: Jeong Sik Lim, Jeongsoon Lee, Seungnam Park

415 Writing – original draft: Jeong Sik Lim, Beni Adi Trisna

Writing – review & editing: Jeong Sik Lim, Beni Adi Trisna

Funding acquisition: Jeong Sik Lim, Jeongsoon Lee

Competing Interests

The authors declare that they have no conflict of interest.

420 **Disclaimer**

Publisher's note: Copernicus Publications remains neutral with regard to jurisdictional claims in published maps and institutional affiliations.

Acknowledgments

We thank Dr. Chu-Shik Kang for providing traceability to the reference cell length measurements. Beni Adi Trisna is grateful
425 to Mr. Sangwoo Kim and Ms. Yera Kim for their fruitful discussions and insights.

Financial support

This work was funded by KRISS as a part of a project for establishing measurement standards for climate monitoring based on molecular spectroscopy (22011102). This work was also supported by the Ministry of Trade, Industry and Energy, Republic of Korea, under projects of laser-based radical measurements for the prediction of atmospheric lifetimes of GHGs used in the
430 semiconductor industry (22201050) and GWP 1,000 or Less Chamber Cleaning Gas and its Remote Plasma System for Low GWP Gas (RS-2022-00155753).

References

- 435 Allen, M. R., Shine, K. P., Fuglestedt, J. S., Millar, R. J., Cain, M., Frame, D. J., Macey, A. H.: A solution to the misrepresentations of CO₂-equivalent emissions of short-lived climate pollutants under ambitious mitigation, *NPJ Climate and Atmospheric Science*, 1, 1-8, <https://doi.org/10.1038/s41612-018-0026-8>, 2018.
- Beni, A. T., Park, S. Park, I. Lee, J. Lim. J. S.: Measurement report: Radiative efficiency estimates of (CF₃)₂CFCN, CF₃OCFCF₂, and CF₃OCF₂CF₃ using high-resolution Fourier transform infrared spectroscopy, <https://doi.org/10.5281/zenodo.7132870>, 2022.
- 440 Bravo, I., Aranda, A., Hurley, M. D., Marston, G., Nutt, D. R., Shine, K. P., Smith, K., Wallington, T. J.: Infrared absorption spectra, radiative efficiencies, and global warming potentials of perfluorocarbons: Comparison between experiment and theory, *Journal of Geophysical Research Atmospheres*, 115, D24317, <https://doi.org/10.1029/2010JD014771>, 2010.
- Denison, S., Forster, P. M., Smith, C. J.: Guidance on emissions metrics for nationally determined contributions under the Paris Agreement, *Environmental Research Letter*, 14, 124002, <https://doi.org/10.1088/1748-9326/ab4df4>, 2019.
- 445 Fleisher, A. J., Adkins, E. M., Reed, Z. D., Yi, H., Long, D. A., Fleurbaey, H. M., Hodges, J. T.: Twenty-five-fold reduction in measurement uncertainty for a molecular line intensity, *Physics Review Letter*, 123, 043001, <https://doi.org/10.1103/PhysRevLett.123.043001>, 2019.
- Forster, P. *et al.*: IPCC sixth assessment report (AR6) working group 1: the physical science basis, chapter 7, University Press, UK, www.ipcc.ch/report/ar6/wg1/downloads, 2021.
- 450 Gordon, I. E., Rothman, L. S., Hill, C., Kochanov, R. V., Tan, Y., Bernath, P. F., Birk, M., Boudon, V., Campargue, A., Chance, K.: The HITRAN2016 molecular spectroscopic database, *Journal of Quantitative Spectroscopy and Radiative Transfer*, 203, 3-69, <https://doi.org/10.1016/j.jqsrt.2017.06.038>, 2017.
- Harrison, J. J., Allen, N. D., Bernath, P. F.: Infrared absorption cross sections for ethane (C₂H₆) in the 3 μm region, *Journal of Quantitative Spectroscopy and Radiative Transfer*, 111, 357-363, <https://doi.org/10.1016/j.jqsrt.2009.09.010>, 2010.
- 455 Harrison, J. J.: Infrared absorption cross sections for 1,1,1,2-tetrafluoroethane, *Journal of Quantitative Spectroscopy and Radiative Transfer*, 151, 210-216, <https://doi.org/10.1016/j.jqsrt.2014.09.023>, 2015.
- Harrison, J. J.: New infrared absorption cross sections for the infrared limb sounding of sulfur hexafluoride (SF₆), *Journal of Quantitative Spectroscopy and Radiative Transfer*, 254, 107202, <https://doi.org/10.1016/j.jqsrt.2020.107202>, 2020.
- 460 Hase, F., Blumenstock, T., Paton-Walsh, C.: Analysis of the instrumental line shape of high-resolution Fourier transform IR spectrometers with gas cell measurements and new retrieval software, *Applied Optics*, 38, 3417-3422, <https://doi.org/10.1364/AO.38.003417>, 1999.
- Hashemi, R., Gordon, I. E., Adkins, E. M., Hodges, J. T., Long, D. A., Birk, M., Loos, J., Boone, C. D., Fleisher, A. J., Predoi-Cross, A., Rothman, L. S.: Improvement of the spectroscopic parameters of the air- and self-broadened NO and CO lines for the HITRAN2020 database applications, *Journal of Quantitative Spectroscopy and Radiative Transfer*, 271, 107735, <https://doi.org/10.1016/j.jqsrt.2021.107735>, 2021.
- 465 Hodnebrog, Ø., Etmann, M., Fuglestedt, J. S., Marston, G., Myhre, G., Nielsen, C. J., Shine, K. P., Wallington, T. J.: Global warming potentials and radiative efficiencies of halocarbons and related compounds: A comprehensive review, *Review of Geophysics*, 51, 300-378, <https://doi.org/10.1002/rog.20013>, 2013.
- 470 Hodnebrog, Ø., Aamaas, B., Fuglestedt, J. S., Marston, G., Myhre, G., Nielsen, C. J., Sandstad, M., Shine, K. P., Wallington, T. J.: Updated global warming potentials and radiative efficiencies of halocarbons and other weak atmospheric absorbers, *Review of Geophysics*, 58, e2019RG000691, <https://doi.org/10.1029/2019RG000691>, 2020.

- 475 Hurley, M., Wallington, T., Buchanan, G., Gohar, L., Marston, G., Shine, K.: IR spectrum and radiative forcing of CF₄ revisited, *Journal of Geophysical Research Atmospheres*, 110, D02102, <https://doi.org/10.1029/2004JD005201>, 2005.
- Jain, A. K., Briegleb, B. P., Minschwaner, K., Wuebbles, D. J.: Radiative forcings and global warming potentials of 39 greenhouse gases, *Journal of Geophysical Research Atmospheres*, 105, 20773-20790, <https://doi.org/10.1029/2000JD900241>, 2000.
- 480 JCGM 100:2008, Evaluation of measurement data—guide for the expression of uncertainty in measurement, Joint Committee for Guides in Metrology (JCGM/WG1), BIPM, France, https://www.bipm.org/documents/20126/2071204/JCGM_100_2008_E.pdf/cb0ef43f-baa5-11cf-3f85-4dcd86f77bd6, 2008.
- Johnson, T. J., Hughey, K. D., Blake, T. A., Sharpe, S. W., Myers, T. L., Sams, R. L.: Confirmation of PNNL
485 quantitative infrared cross-sections for isobutane, *Journal of Physical Chemistry A*, 125, 3793-3801, <https://doi.org/10.1021/acs.jpca.1c01933>, 2021.
- Kim, J. W., Yoo, Y. S., Lee, J. Y., Lee, J. B., Hahn, J. W.: Uncertainty analysis of absolute concentration measurement with continuous-wave cavity ringdown spectroscopy, *Applied Optics*, 40, 5509-5516, <https://doi.org/10.1364/AO.40.005509>, 2001.
- 490 Kim, J., Lee, J.: Estimation of the global warming potential of fluorinated green house gases, *Journal of Korean Society for Atmospheric Environment*, 30, 387-397, <https://doi.org/10.5572/KOSAE.2014.30.4.387>, 2014.
- Kovács, T., Feng, W., Totterdill, A., Plane, J., Dhomse, S., Gómez-Martín, J. C., Stiller, G. P., Haenel, F. J., Smith, C., Forster, P. M.: Determination of the atmospheric lifetime and global warming potential of sulfur hexafluoride using a three-dimensional model, *Atmospheric Chemistry and Physics*, 17, 883-898, <https://doi.org/10.5194/acp-17-883-2017>,
495 2017.
- Laruelle, E., Kieffel, Y., Ficheux, A.: In international conference on eco-design in electrical engineering, Springer, 139-146, <https://link.springer.com/book/10.1007/978-3-319-58172-9>, 2017.
- Li, Z., Tao, Z., Naik, V., Good, D. A., Hansen, J. C., Jeong, G. R., Francisco, J. S., Jain, A. K., Wuebbles, D. J.: Radiative forcings and global warming potentials of 39 greenhouse gases, *Journal of Geophysical Research Atmospheres*, 105, 4019-4029, <https://doi.org/10.1029/2000JD900241>, 2000.
500
- Loos, J., Birk, M., Wagner, G.: Pressure broadening, -shift, speed dependence and line mixing in the v₃ rovibrational band of N₂O, *Journal of Quantitative Spectroscopy and Radiative Transfer*, 151, 300-309, <https://doi.org/10.1016/j.jqsrt.2014.10.008>, 2015.
- Lynch, J., Cain, M., Pierrehumbert, R., Allen, M.: Demonstrating GWP*: a means of reporting warming-equivalent
505 emissions that captures the contrasting impacts of short- and long-lived climate pollutants, *Environmental Research Letter*, 15, 044023, <https://doi.org/10.1088/1748-9326/ab6d7e>, 2020.
- Nelson, C. T., Overzet, L. J., Goeckner, M. J.: Temperature dependence of the infrared absorption cross-sections of neutral species commonly found in fluorocarbon plasmas, *Journal of Vacuum Science & Technology A*, 30, 021305, <https://doi.org/10.1116/1.3679408>, 2012.
- 510 Nwaboh, J. A., Witzel, O., Pogány, A., Werhahn, O., Ebert, V.: Optical path length calibration: a standard approach for use in absorption cell-based IR-spectrometric gas analysis, *International Journal of Spectroscopy*. ID 132607, <https://doi.org/10.1155/2014/132607>, 2014.
- Pagliano, E., Meija, J.: Reducing the matrix effects in chemical analysis: fusion of isotope dilution and standard addition methods, *Metrologia*, 53, 829-834, <https://doi.org/10.1088/0026-1394/53/2/829>, 2016.
- 515 Pan, B., Wang, G., Shi, H., Shen, J., Ji, H.-K., Kil, G.-S.: Green gas for grid as an eco-friendly alternative insulation gas to SF₆: a review, *Applied Science*, 10, 2526, <https://doi.org/10.3390/app10072526>, 2020.

- Pinnock, S., Hurley, M. D., Shine, K. P., Wallington, T. J., Smyth, T.: Radiative forcing of climate by hydrochlorofluorocarbons and hydrofluorocarbons, *Journal of Geophysical Research Atmospheres*, 100, 23227-23238, <https://doi.org/10.1029/95JD02323>, 1995.
- 520 Pinnock, S., Shine, K. P.: The effects of changes in HITRAN and uncertainties in the spectroscopy on infrared irradiance calculations, *Journal of Atmospheric Sciences*, 55, 1950-1964, [https://doi.org/10.1175/1520-0469\(1998\)055<1950:TEOCIH>2.0.CO;2](https://doi.org/10.1175/1520-0469(1998)055<1950:TEOCIH>2.0.CO;2), 1998.
- Rhoderick, G., Guenther, F., Duewer, D., Lee, J., Moon, D., Lee, J., Lim, J. S., Kim, J. S.: Final report on international comparison CCQM-K83: Halocarbons in dry whole air, *Metrologia*, 51, 08009, <https://doi.org/10.1088/0026-1394/51/1A/08009>, 2014.
- 525 Robson, J., Gohar, L., Hurley, M., Shine, K., Wallington, T.: Revised IR spectrum, radiative efficiency and global warming potential of nitrogen trifluoride, *Geophysics Research Letter*, 33, L10817, <https://doi.org/10.1029/2006GL026210>, 2006.
- Rosenzweig, C., Ruane, A. C., Antle, J., Elliott, J., Ashfaq, M., Chatta, A. A., Ewert, F., Folberth, C., Hathie, I., Havlik, P.: Coordinating AgMIP data and models across global and regional scales for 1.5°C and 2.0°C assessments, *Philosophical Transactions of the Royal Society A*. 376, 20160455, <https://doi.org/10.1098/rsta.2016.0455>, 2018.
- 530 Shine, K. P., Myhre, G.: The spectral nature of stratospheric temperature adjustment and its application to halocarbon radiative forcing, *Journal of Advances in Modeling Earth Systems*, 12, e2019MS001951, <https://doi.org/10.1029/2019MS001951>, 2020.
- 535 Smith, T., Wooster, M., Tattaris, M., Griffith, D.: Absolute accuracy and sensitivity analysis of OP-FTIR retrievals of CO₂, CH₄ and CO over concentrations representative of "clean air" and "polluted plumes", *Atmospheric Measurement Techniques*, 4, 97-116, <https://doi.org/10.5194/amt-4-97-2011>, 2011.
- Sulbaek Andersen, M. P., Kyte, M., Andersen, S. T., Nielsen, C. J., Nielsen, O. J.: Atmospheric chemistry of (CF₃)₂CF=C≡N: a replacement compound for the most potent industrial greenhouse gas, SF₆, *Environmental Science and Technology*, 51, 1321-1329, <https://doi.org/10.1021/acs.est.6b03758>, 2017.
- 540 Sulbaek Andersen, M. P., Nielsen, O. J., Sherman J. D.: The global warming potentials for anesthetic gas sevoflurane need significant corrections, *Environmental Science and Technology*, 55, 10189-10191, <https://doi.org/10.1021/acs.est.1c02573>, 2021.
- UNFCCC secretariat: Report of the conference of the parties on its twenty-first session, part two: action taken by the conference of the parties at its twenty-first session, United Nations Framework Convention on Climate Change (UNFCCC), UN: NYC, <https://unfccc.int/process-and-meetings/conferences/past-conferences/paris-climate-change-conference-november-2015/cop-21/cop-21-reports>, 2015.
- 545 Zhao, M., Han, D., Zhou, Z., Zhang, G.: Experimental and theoretical analysis on decomposition and by-product formation process of (CF₃)₂CFCN mixture, *AIP Advances*. 9, 105204, <https://doi.org/10.1063/1.5116211>, 2019